We are IntechOpen, the world's leading publisher of Open Access books Built by scientists, for scientists

4,800
Open access books available

122,000
International authors and editors

135M
Downloads

Our authors are among the

154
Countries delivered to

TOP 1%
most cited scientists

12.2%
Contributors from top 500 universities

WEB OF SCIENCE™

Selection of our books indexed in the Book Citation Index
in Web of Science™ Core Collection (BKCI)

Interested in publishing with us?
Contact book.department@intechopen.com

Vorticity Evolution near the Turbulent/Non-Turbulent Interfaces in Free-Shear Flows

Tomoaki Watanabe, Koji Nagata and
Carlos B. da Silva

Abstract

Vorticity dynamics is studied near the interface between turbulent and non-turbulent flows, the so-called turbulent/non-turbulent (T/NT) interface, with the direct numerical simulations of planar jets and mixing layers. The statistics near the interface confirm that the T/NT interface consists of two layers: viscous superlayer and turbulent sublayer. The viscous superlayer with the thickness of four times of Kolmogorov length scale is found at the outer edge of the interface, where the vorticity grows with the viscous diffusion. In the turbulent sublayer between the viscous superlayer and the turbulent region, the strain-vorticity interaction becomes active. In the Lagrangian statistics for the fluid particles, the different scaling laws appear in the entrained particle movement depending on the layer: a ballistic evolution in the viscous superlayer and the Richardson-like scaling for relative dispersion in the turbulent sublayer. These scalings indicate that the change in the particle position in the viscous superlayer is governed by the outward viscous diffusion of vorticity, whereas it is governed by the inviscid small-scale eddy motions in the turbulent sublayer. The flow topology on the particle path line shows that the fluid being entrained tends to circumvent the core region of intense eddies near the T/NT interface.

Keywords: jet, mixing layer, turbulent/non-turbulent interface, DNS, Lagrangian statistics

1. Introduction

Interfaces dividing turbulent and non-turbulent regions appear in various canonical turbulences, such as boundary layers, jets, and mixing layers, where turbulence is generated from the shear due to the wall friction or mean velocity difference. These interfaces are called turbulent/

non-turbulent (T/NT) interfaces. Turbulence is generated by shear motions in various circumstances, where the turbulent fluids are surrounded by non-turbulent fluids. This locally generated turbulence often plays an important role in the relevant phenomena. For example, ocean-mixing layers [1], generated in the stably stratified fluid, are sometimes responsible for the transport of heat, salinity, and plankton. The atmospheric boundary layer [2] is related to the cooling/heating of the ground surface and the transport of contaminant. In the flows with the T/NT interface, the turbulent region grows into the non-turbulent region with the mass, momentum, and energy exchanges across the T/NT interface.

Corrsin and Kistler [3], in laboratory experiments with hot-wire probes, found that the essential feature of the turbulent regions is the high vorticity, and the turbulent and non-turbulent regions can be distinguished by the vorticity. They also predicted that a very thin layer where the non-turbulent fluids acquire vorticity by the viscous diffusion is formed at the outer edge of the turbulent region. This thin layer, called the viscous superlayer, was confirmed with the recent high-resolution direct numerical simulations (DNSs) [4]. Furthermore, the statistical approach conditioned relative to the interface [5] clearly showed that the T/NT interface is the layer with a finite thickness. In addition to the viscous superlayer, an adjacent layer, turbulent sublayer, was found between the turbulent core region and the viscous superlayer [6]. One of the differences between the turbulent sublayer and the viscous superlayer is in the vorticity dynamics; the initial growth of vorticity of the non-turbulent fluid occurs by the viscous diffusion in the viscous superlayer with the absence of inviscid vortex stretching, whereas the vortex stretching plays an important role in the amplification of vorticity in the turbulent sublayer [7,8].

The T/NT interface has been studied in particular attention to the entrainment process since this is where the non-turbulent fluid acquires vorticity and results in the transition to turbulence. Turbulent flows consist of the motions in a wide range of scales, and both small and large scales can cause the entrainment by nibbling [9] and engulfment [10], respectively. The experiments in the boundary layers indicated that the entrainment is the multi-scale process [11]. The entrainment across the interface was studied in [12] with the propagation velocity of the enstrophy isosurface. These analyses on the isosurface movement showed that the propagation velocity is of the order of the Kolmogorov velocity $v_\eta = (v\varepsilon)^{1/4}$ [13,14], where v is the kinematic viscosity and ε is the dissipation rate of turbulent kinetic energy, and the complex shape of the isosurface [15] relates the propagation velocity to the total entrainment rate, which can be written as a function of large-scale quantities [16]. The enstrophy isosurface is an infinitely thin surface located within the T/NT interface layer. Therefore, a more precise description of the entrainment process is the fluid movement across the entire T/NT interface layer than across the enstrophy isosurface. During the entrainment, the irrotational particles pass both the viscous superlayer and the turbulent sublayer. The Lagrangian analysis is useful for studying the entrainment, and both experiments and simulations have been used for tracking the fluid particles (tracers) being entrained from the non-turbulent regions [14,17,18]. These studies showed the evolution of turbulence characteristics during the entrainment. However, the relation between these Lagrangian statistics and the layer structures is not clear

because the particle tracking does not show the location within the T/NT interface layer because the T/NT interface also moves with the convective fluid motion.

In this study, we explore the connection between the T/NT interface structure and the Lagrangian statistics during the entrainment process based on our recent DNS results [19]. The DNS is performed for mixing layers and planar jets, and used for tracking the fluid particles being entrained. In addition to the fluid particles, the outer edge of the T/NT interface layer, defined by the enstrophy isosurface, is also tracked with the Lagrangian markers, enabling us to examine the location of the fluid particle within the T/NT interface layer and to relate the Lagrangian statistics to the Eulerian counterparts. The roles of small-scale eddy structures in the entrainment are considered from the Lagrangian and Eulerian statistics. This chapter is organized as follows: Section 2 presents the numerical methods and parameters as well as the conventional statistics for the validation of the DNS data. Section 3 discusses the analysis on the T/NT interface, such as the interface detection, and the conditional analysis based on the Eulerian and Lagrangian statistics. Finally, Section 4 closes the chapter with the conclusion.

2. Direct numerical simulations

Direct numerical simulations are performed for temporally evolving mixing layers and planar jets [19]. These flows develop from the initial state in the computational domain, which is periodic in the mean flow (x) and spanwise (z) directions. The flows spread in the cross-streamwise (y) direction. We consider the computational box with the size of ($L_x \times L_y \times L_z$) represented by ($N_x \times N_y \times N_z$) grid points. The boundaries in the y direction are treated as the slip wall [7]. The origin of the coordinate system is at the center of the computational domain. The DNS code is an incompressible Navier-Stokes solver based on the fractional step method [8]. In addition to the flow field, a passive scalar ϕ is simulated with the convection-diffusion equation. The governing equations are spatially discretized with a fully conservative finite-difference method [20]. The second-order and fourth-order schemes are used in the cross-streamwise and the periodic directions, respectively. The governing equations are integrated in time with a third-order Runge-Kutta method. The Poisson equation is solved with the fast Fourier transform along the periodic directions and the diagonal matrix algorithm along the x direction.

The initial velocity field is obtained by superimposing the statistically homogeneous and isotropic velocity fluctuations onto the mean velocity, which is given by

$$\langle U \rangle = 0.5 U_{\mathrm{M}} \tanh\left(\frac{2y}{\theta_{\mathrm{M}}}\right) \text{ in mixing layers,} \tag{1}$$

$$\langle U \rangle = 0.5 U_{\mathrm{J}} + 0.5 U_{\mathrm{J}} \tanh\left(\frac{H - 2\,|\,y\,|}{4\theta_{\mathrm{J}}}\right) \text{ in planar jets.} \tag{2}$$

Here, U_M is the velocity difference in the mixing layers, U_J the jet velocity, H the width of the jet inlet and θ_M (θ_J) the initial shear layer thickness in the mixing layers (planar jets). The angular bracket denotes the averaged value in a $x - y$ plane. We set $\theta_J = 0.015H$. The initial velocity fluctuations are generated by a diffusion process [21], where the characteristics length scales are $0.07H$ in the planar jets and $0.25\delta_M$ in the mixing layers. The initial rms velocity is $0.04U_J$ for $|y|/H \leq 0.5$ in the planar jets and is $0.025U_M$ for $|y|/\delta_M \leq 3$ in the mixing layer. Except these regions, the fluctuations are not imposed on the mean velocity. The initial scalar profiles are given by

$$\phi = 0.5\tanh\left(\frac{2y}{\theta_M}\right) \text{ in mixing layers,} \tag{3}$$

$$\phi = 0.5 + 0.5\tanh\left(\frac{H - 2|y|}{4\theta_J}\right) \text{ in planar jets.} \tag{4}$$

| Run	ML04	ML08	PJ50	PJ90
Flow type	Mixing layer	Mixing layer	Planar jet	Planar jet
Re	400	800	5000	9000
L_x	$16\pi\theta_M$	$16\pi\theta_M$	$2.4\pi H$	$2.6\pi H$
L_y	$16\pi\theta_M$	$16\pi\theta_M$	$4.8\pi H$	$3.8\pi H$
L_z	$8\pi\theta_M$	$8\pi\theta_M$	$2.4\pi H$	$1.3\pi H$
N_x	512	1 024	512	1 024
N_y	500	700	850	1 150
N_z	256	512	512	512
Time step dt	$0.08\theta_M/U_M$	$0.04\theta_M/U_M$	$0.012H/U_J$	$0.006H/U_J$
$\Delta_x = \Delta_z$	1.5η	1.2η	1.5η	1.4η
Δ_y ($y = 0$)	1.0η	1.1η	1.2η	1.2η
Re_λ	105	151	94	158
η	$0.064\theta_M$	$0.041\theta_M$	$0.0096H$	$0.0059H$
λ	20.8η	23.3η	14.8η	20.3η

Table 1. Physical and computational parameters of the DNS. The displayed turbulence characteristics are from the turbulent core regions.

The Reynolds numbers Re are defined by $U_M\theta_M/\nu$ and U_JH/ν. We perform the DNS for the planar jets with Re = 5 000 and 9 000 and for the mixing layers with Re = 400 and 800. The Schmidt number of ϕ is $Sc = \nu/D = 1$, where D is the molecular diffusivity. **Table 1** shows the physical and computational parameters, such as the Kolmogorov scale η, Taylor microscale λ_x, and the turbulent Reynolds number Re_λ, where the Taylor microscale and turbulent

Reynolds number are calculated from the streamwise velocity statistics. The computational grid size, Δ_i, is comparable to η, and is able to capture turbulent motions in very small scales.
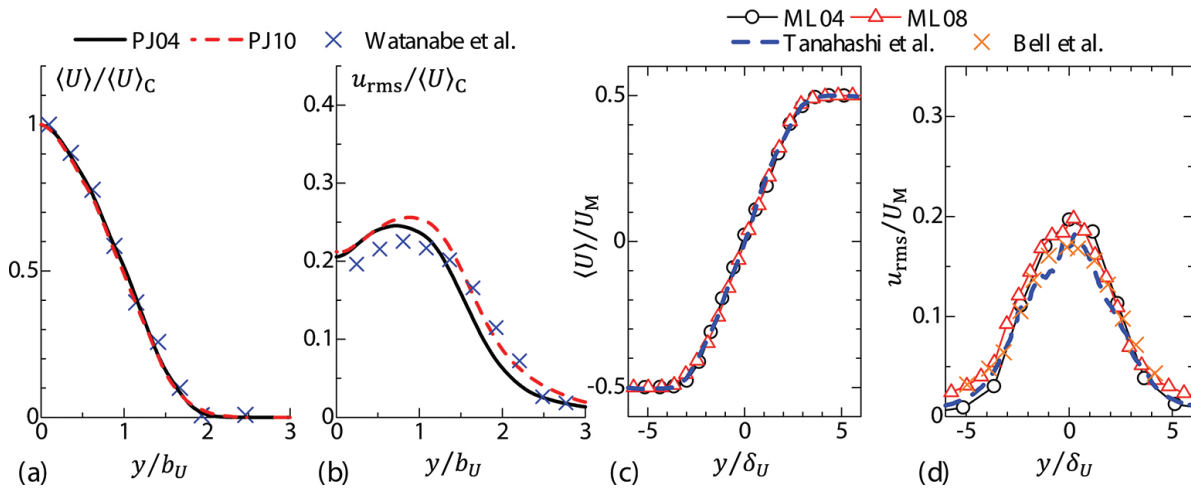
Figure 1. Self-similar profiles of mean streamwise velocity $\langle U \rangle$ and rms streamwise velocity u_{rms} in (a and b) planar jets and (c and d) mixing layers. $\langle U \rangle_C$ and b_U denote the mean streamwise velocity on the centerline and the jet half-width obtained from $\langle U \rangle$, respectively. The mixing layer thickness δ_U is defined as $\delta_U = \int (0.5U_M - \langle U \rangle)(\langle U \rangle - 0.5U_M)/(U_M)^2 dy$. The present DNS results are compared with the experiments and DNS on the planar jets [22] and mixing layers [23,24].
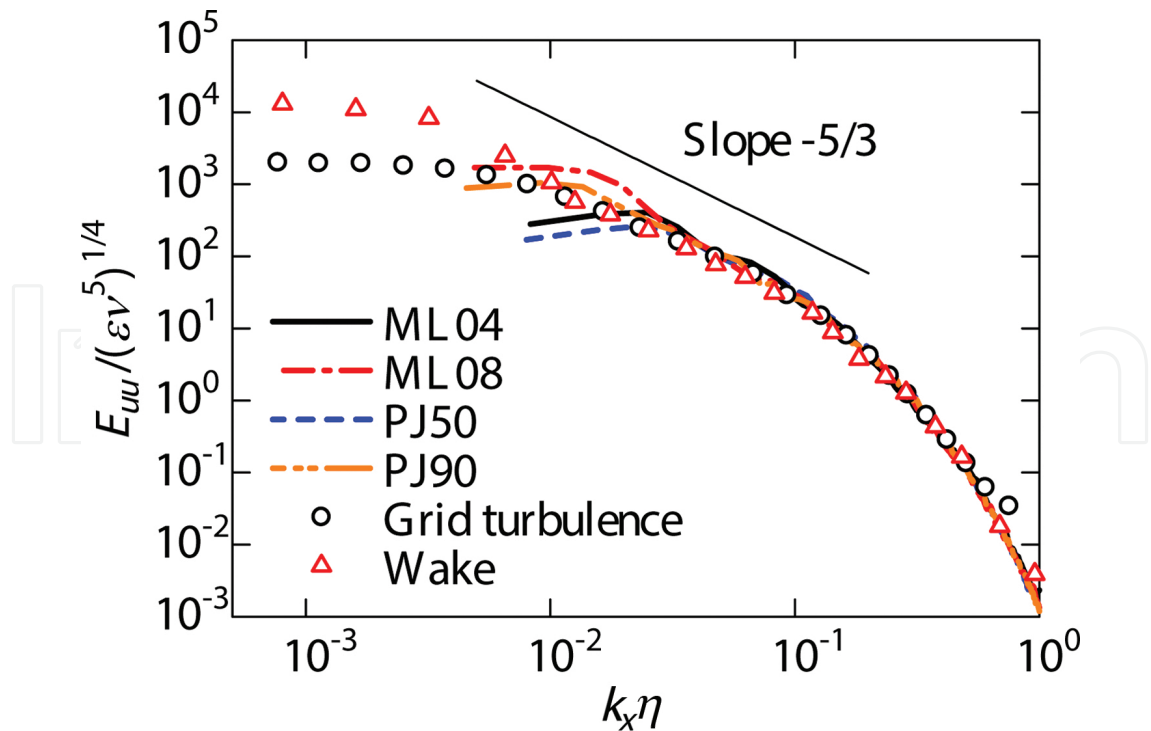

Figure 2. One-dimensional longitudinal spectrum E_{uu} on the centerline of the planar jets and mixing layers compared with the experimental plots in grid turbulence [25] and axisymmetric wake [26].

The fundamental characteristics of the planar jets and mixing layers are compared with other DNS and experiments for validation of the DNS. **Figure 1** compares the self-similar profiles of mean velocity and rms velocity fluctuations. The present DNS reproduces well the self-similar profiles of these statistics in previous studies. **Figure 2** shows the one-dimensional longitudinal spectrum on the centerline with the experimental plots. We can see the overlap of the spectrum in small scales, and the small-scale turbulent fluctuations are well resolved in the DNS.

3. Analysis on turbulent and non-turbulent interface

3.1. Detection of the T/NT interface

The turbulent regions are characterized by high vorticity [3]. Therefore, following [5], we define the turbulent region as where the vorticity magnitude $|\omega|$ exceeds the threshold ω_{th}. Then, with an appropriate value of ω_{th}, the isosurface of $|\omega| = \omega_{th}$ can be detected so that it is located near the outer edge of the T/NT interface layer. The specific value of ω_{th} is obtained from a well-known dependence of turbulent volume on ω_{th} [18]. **Figure 3(a)** shows the volume fraction of turbulent regions as a function of ω_{th}. We can see a plateau in the turbulent volume, and the isosurface location hardly changes with ω_{th} for the plateau. We choose $\omega_{th} = 0.04\langle|\omega|\rangle_C$, which is from the plateau shown in **Figure 3(a)**. This value is chosen so that the isosurface is located at the outer edge of the T/NT interface layer. We call this isosurface as the *irrotational boundary* hereafter. **Figure 3(b)** and **(c)** show the enstrophy profile and the irrotational boundary. The irrotational boundary surrounds the high enstrophy region and is located at the outer edge of the turbulent fluids. Thus, the outer edge of the T/NT interface layer is well defined by thresholding the vorticity magnitude.
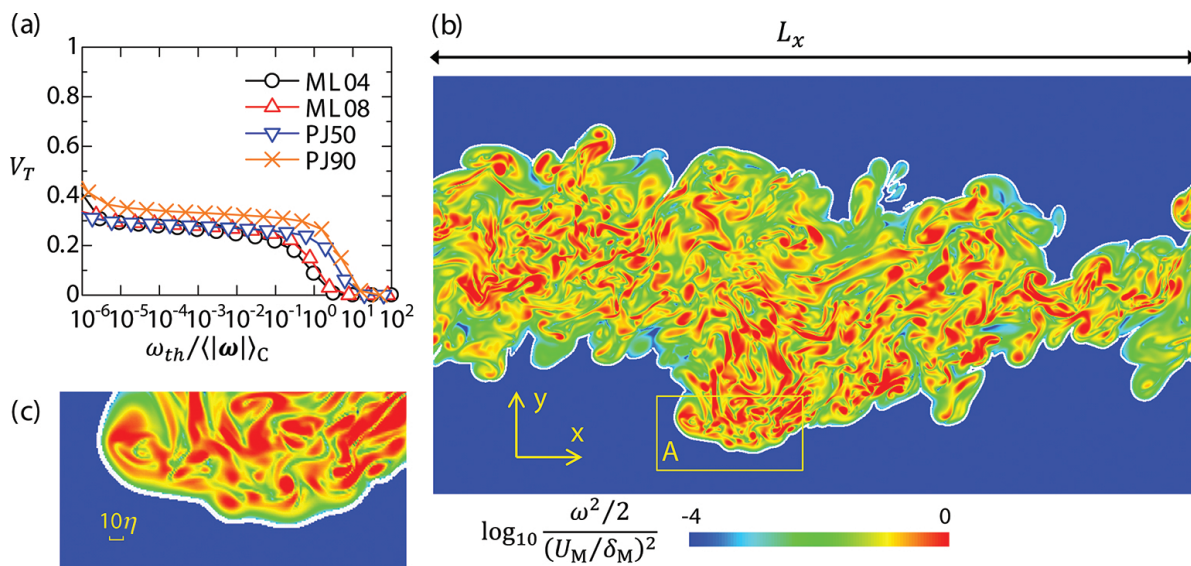
Figure 3. Detection of the T/NT interface. (a) Dependence of the turbulent volume fraction on the normalized threshold $\omega_{th}/\langle\omega\rangle_C$. (b) Visualization of the irrotational boundary in ML08 (white line). The color contours show enstrophy levels in $\log_{10}(\omega^2/2)$. (c) The close-up of the T/NT interface (the region A in (b)).

The irrotational boundary is visualized in **Figure 4**. The T/NT interface has a very complex shape. The Re dependence is also clear; the higher Re mixing layer has smaller-scale structures because of the small length scales of turbulence.
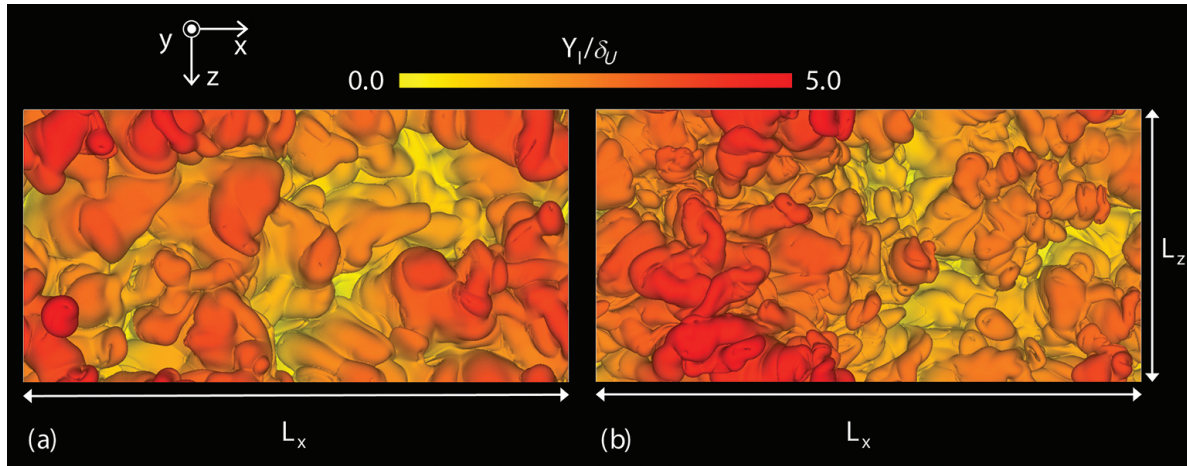
Figure 4. Visualization of the irrotational boundary (the vorticity magnitude isosurface) in the mixing layers with (a) Re = 400 and (b) Re = 800. The color shows the interface height Y_I from the centerline normalized by the mixing layer thickness $\delta_U = \int(0.5U_M - \langle U \rangle)(\langle U \rangle - 0.5U_M)/(U_M)^2 dy$.

3.2. Statistics conditioned on the location of the T/NT interface

The vorticity dynamics is studied with the statistics conditioned on the location from the irrotational boundary. This interface coordinate, ζ_I, is taken in the normal direction of the irrotational boundary $\boldsymbol{n} = -\nabla\omega^2/|\nabla\omega^2|$, where $\zeta_I = 0$ is the location of the irrotational boundary.
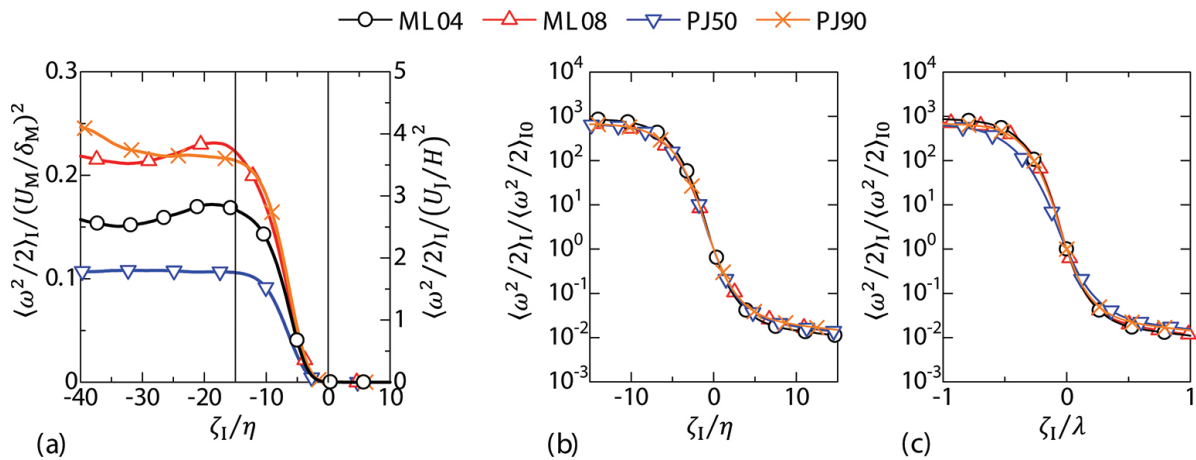
Figure 5. (a) Conditional mean enstrophy $\langle \omega^2/2 \rangle_I$. The vertical lines, from right to left, denote $\zeta_I = 0$ and $\zeta_I = -15\eta$, where $\langle \omega^2/2 \rangle_I$ reaches the value close to the turbulent core region. Conditional mean enstrophy divided by the value at the irrotational boundary $\langle \omega^2/2 \rangle_{I0}$ against the interface coordinate normalized by (b) Kolmogorov scale η and (c) Taylor microscale $\lambda = (\lambda_x + \lambda_y + \lambda_z)$.

The non-turbulent region is indicated by $\zeta_I > 0$. Because of the complicated shape of the T/NT interface, a turbulent (non-turbulent) fluid and an associated irrotational boundary can appear for $\zeta_I > 0$ ($\zeta_I < 0$). For separating the statistics into the turbulent and non-turbulent parts, the statistics are calculated solely from turbulent and non-turbulent regions in $\zeta_I < 0$ and $\zeta_I > 0$, respectively. When another irrotational boundary is found at $\zeta_I \neq 0$, the region within the distance of λ from this boundary is excluded from the statistics for preventing the T/NT interface layer from affecting the statistics for $\zeta_I \gg 0$ or $\ll 0$. Note that previous studies have shown that the T/NT interface layer thickness is about 0.5λ [27]. Hereafter, $\langle \rangle_I$ denotes the conditional mean value.

Figure 5 shows the conditional mean enstrophy profiles. The mean enstrophy is matched in the layer with the thickness of $\approx 15\eta$. The scaling of the thickness of the interface layer is examined in the plots of $\langle \omega^2/2 \rangle_I$ normalized by the value at $\zeta_I = 0$, $\langle \omega^2/2 \rangle_{I0}$, in **Figure 5(b)** and **(c)**, where ζ_I is normalized by the Kolmogorov scale η and Taylor microscale λ, respectively. The plots tend to better collapse onto a single curve for ζ_I/η than ζ_I/λ, and thus the thickness of the T/NT interface layer, across which the enstrophy changes, is scaled with the Kolmogorov scales. It should be noted that the Taylor microscale can be the characteristics length scale of the T/NT interface when the large-scale coherent structures exist near the T/NT interface [28].
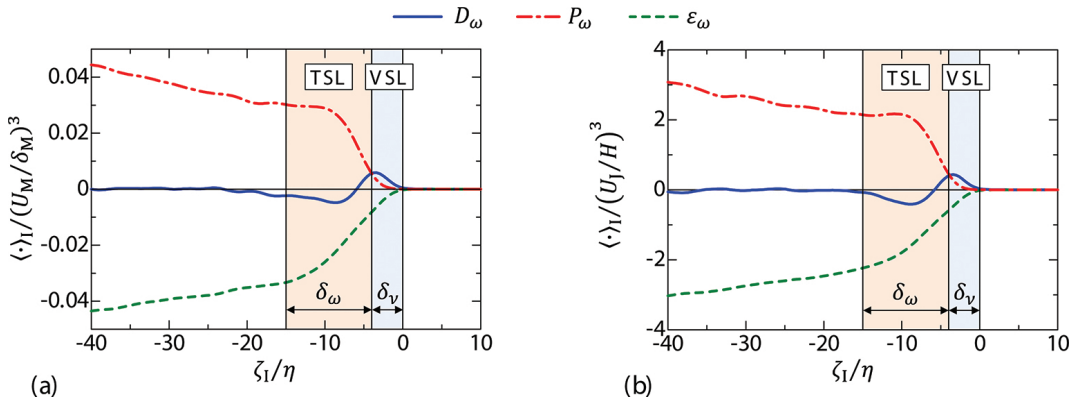
Figure 6. Conditional enstrophy budget in (a) ML08 and (b) PJ90, where $D_\omega = \nu \nabla^2 \omega^2/2$ is the viscous diffusion term, $P_\omega = \omega_i S_{ij} \omega_j$ is the production term, $\varepsilon_\omega = - \nu \nabla \omega_j \cdot \nabla \omega_j$ is the viscous dissipation term. The vertical lines, from right to left, denote $\zeta_I = 0$, $\zeta_I = - 4\eta$, where $\langle D_\omega \rangle_I = \langle P_\omega \rangle_I$, and $\zeta_I = - 15\eta$. The viscous superlayer (VSL) with the thickness δ_v and the turbulent sublayer (TSL) with the thickness δ_ω are highlighted.

The vorticity evolution near the interface is studied by the enstrophy transport equation:

$$\frac{D\omega^2/2}{Dt} = \omega_i S_{ij}\omega_j + \nu\nabla^2(\omega^2/2) - \nu\nabla\omega_i \cdot \nabla\omega_i, \tag{5}$$

where the first term on the right-hand side is the enstrophy production P_ω (S_{ij}: strain-tensor), the second is the viscous diffusion D_ω, and the third is the viscous dissipation ε_ω. The conditional average of each term is plotted in **Figure 6** for ML08 and PJ90. The plots are very similar for these flows in the T/NT interface layer; the enstrophy grows by the viscous diffusion near

the outer edge of the T/NT interface, whereas the inviscid vortex stretching becomes important slightly inside the outer edge. The profile of $\langle D_\omega \rangle_I$ exhibits negative and positive values in the T/NT interface layer, indicating the vorticity transport toward the non-turbulent region. Near the outer edge of the T/NT interface layer, $\langle D_\omega \rangle_I$ is larger than $\langle P_\omega \rangle_I$ in the region of $-4\eta \le \zeta \le 0$. This thickness, $\delta_v = 4\eta$, agrees with the direct observation of the viscous superlayer thickness [4]. Thus, from the conditional mean profiles of enstrophy and its budget, we can identify the viscous superlayer in $-4\eta \le \zeta_I \le 0$ and the adjutant layer, turbulent sublayer, with the thickness of $\delta_\omega = 11\eta$ in $-15\eta \le \zeta_I \le -4\eta$. This structure of the T/NT interfaces is observed in all DNS dataset. In the turbulent core region, the mean enstrophy production $\langle P_\omega \rangle_I$ almost balances with the mean viscous dissipation $\langle \varepsilon_\omega \rangle_I$. This balance is absent in the T/NT interface layer; from $\zeta_I = -15\eta$, $\langle \varepsilon_\omega \rangle_I$ becomes small toward the irrotational boundary, whereas $\langle P_\omega \rangle_I$ hardly changes with the location for $-15\eta \le \zeta_I \le -9\eta$.

Figure 7 gives the conditional plots of passive scalar ϕ and scalar dissipation rate $\chi = D \nabla \phi \cdot \nabla \phi$. In the mixing layer, the conditional statistics are calculated from the upper interface, for which the non-turbulent fluid has $\phi = 0.5$, where the upper interface is detected as the irrotational boundary with $\nabla \omega^2 \cdot \nabla \phi < 0$. The conditional mean scalar, $\langle \phi \rangle_I$, also changes in the T/NT interface layer, and is adjusted between the turbulent and non-turbulent regions. The jump in $\langle \phi \rangle_I$ is very similar in all DNS, and the thickness of this jump scales with the Kolmogorov scale at $Sc = 1$ and in the Re range studied here. Because of the difference in $\langle \phi \rangle$ between the turbulent and non-turbulent regions, the scalar gradient becomes large in the T/NT interface layer. Therefore, as shown in **Figure 7(b)**, the scalar dissipation has a large peak at $\zeta_I = -4.9\eta$ in the T/NT interface layer. This location is shown in **Figure 7(a)** by the vertical line, and is close to the inflection point of $\langle \phi \rangle_I$ and to the boundary between the viscous superlayer and the turbulent sublayer.
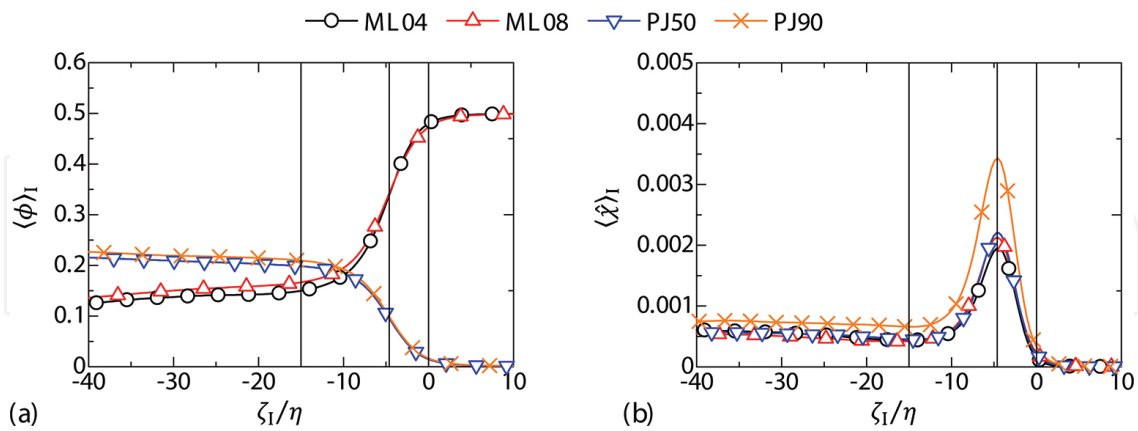
Figure 7. Conditional mean scalar (ϕ) and normalized scalar dissipation rate ($\hat{\chi}$), where $\hat{\chi} = (\delta_M^2 / ReSc)\nabla\phi \cdot \nabla\phi$ in the mixing layers and $\hat{\chi} = (H^2 / ReSc)\nabla\phi \cdot \nabla\phi$ in the planar jets. The vertical lines, from right to left, denote $\zeta_I = 0$, $\zeta_I = -4.9\eta$, where $\langle \hat{\chi} \rangle_I$ reaches a peak, and $\zeta_I = -15\eta$.

The strain-rate tensor S_{ij} plays an important role in small-scale dynamics of turbulence. The interaction between strain and vorticity leads to the vortex stretching $\omega_i S_{ij}$, and in turn to

enstrophy production $\omega_i S_{ij} \omega_j$. The gradient of passive scalar, $G_i = \partial\phi/\partial x_i$, is also affected by the strain field via the straining term $-G_i S_{ij}$, which appears as the production term of χ. The effective strains acting on the vorticity and the scalar gradient are written as follows [29]:

$$\alpha_\omega = \frac{\omega_i S_{ij} \omega_j}{\omega_k \omega_k},\tag{6}$$

$$\gamma_\chi = -\frac{G_i S_{ij} G_j}{G_k G_k},\tag{7}$$

where α_ω and γ_χ are the production rates of enstrophy and of scalar dissipation rate, respectively [30]. Note that the vortex stretching and the compression of the scalar gradient are denoted by positive α_ω and γ_χ, respectively, and positive values of the effective strains contribute to the amplification of enstrophy and of scalar dissipation rate. **Figure 8** shows the conditional average of α_ω and γ_χ normalized by the strain product on the centerline $\langle S_{ij}S_{ij}\rangle_C$. The profiles are almost independent of the flows. $\langle\alpha_\omega\rangle_I$ and $\langle\gamma_\chi\rangle_I$ decrease toward the interface in the turbulent core region, but peaks can be found in the turbulent sublayer, where the amplification of enstrophy and scalar dissipation rate becomes more efficient. This results in a predominance of the enstrophy production over the viscous dissipation in the T/NT interface layer ($\langle P_\omega\rangle_I > |\langle\varepsilon_\omega\rangle_I|$ in **Figure 6**).
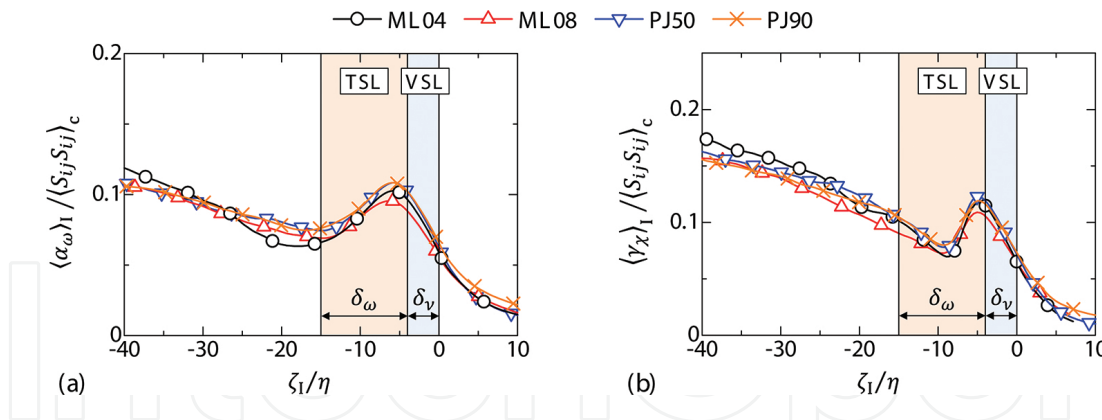
Figure 8. Conditional mean profiles of (a) effective extensive strain acting on vorticity $\alpha_\omega = \omega_i S_{ij}\omega_j/(\omega_k\omega_k)$ and (b) effective compressive strain acting on scalar gradient $\gamma_\chi = -G_i S_{ij}G_j/(G_k G_k)$, where the mean strain product on the centerline $\langle S_{ij}S_{ij}\rangle_C$ is used for normalization. The viscous superlayer and turbulent sublayer are also indicated.

3.3. Lagrangian statistics of entrained fluid particles

The Lagrangian particle tracking is used for investigating the vorticity growth during the entrainment of non-turbulent fluids. Once the flows have reached the self-similar regime, 140,000 particles are seeded in the non-turbulent regions near the irrotational boundary. The particles are tracked with a third-order Runge-Kutta method and a trilinear interpolation

scheme [31]. The flow characteristics are changed depending on the location in the T/NT interface layer. Therefore, it is important to know the entrained fluid particle location within the T/NT interface layer for better understanding of the Lagrangian properties of the entrainment. Because of the T/NT interface movement, the entrained particle tracking does not show the location in the T/NT interface layer. Here, in addition to the fluid particles, the irrotational boundary is also tracked with a marker, which moves with the velocity of the enstrophy isosurface movement u_I. As in **Figure 9(a)**, the marker is placed on the irrotational boundary where the fluid particle has crossed. u_I is the sum of the fluid velocity at the irrotational boundary u_0 and the propagation velocity of the enstrophy isosurface $u_P = v_E n$, where $v_E = (D\omega^2/Dt)/|\nabla\omega^2|$. It was shown that only a negligible fraction of entrained fluid particles is trapped inside a non-turbulent region completely surrounded by turbulent fluids [18]. Because the irrotational boundary of this region disappears after it becomes turbulent, the markers of this irrotational boundary are no longer located on the enstrophy isosurface. Therefore, $|\omega|$ on the markers is monitored at every time step, and markers with $|\omega| > 2\omega_{th}$ are excluded from the subsequent analysis.

The Lagrangian statistics are calculated for the fluid particles, conditioned on the time τ elapsed after a fluid particle has crossed the irrotational boundary, and the Lagrangian conditional average is denoted by $\langle\rangle_\tau$. A separation vector δx is introduced as in **Figure 9(a)**, and is used for examining the particle location in the T/NT interface layer.

Figure 9(b) shows the Lagrangian conditional average of $\delta x = |\delta x|$, where δx and τ are normalized by the Kolmogorov length scale η and time scale τ_η at the time when the fluid particles are seeded. The plots are quite similar for small τ in all DNS. It takes about $7\tau_\eta$ for the entrained particles to reach the turbulent sublayer by moving across the viscous superlayer. A difference in δx becomes clear in the turbulent sublayer; the time needed for the particles to move across the turbulent sublayer changes depending on the flow configuration and Reynolds number. The relation between $\langle\delta x\rangle_\tau$ and τ is used for relating the Lagrangian statistics
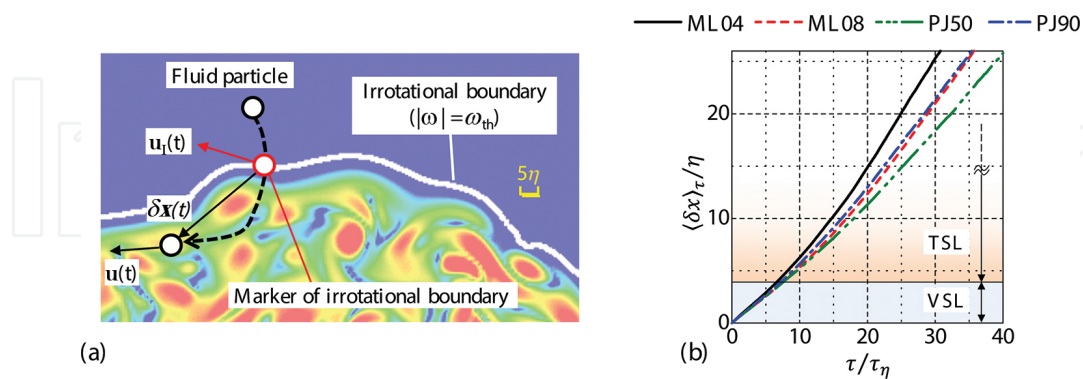
Figure 9. (a) The fluid particle movement is analyzed in relation to the irrotational boundary, which is tracked with a marker moving with the velocity of the enstrophy isosurface movement. A marker is introduced at the boundary where the fluid particle crosses. The irrotational boundary is indicated by a white line while enstrophy levels are shown with the color contours. (b) Conditional mean distance between the entrained fluid and the irrotational boundary marker $\langle|\delta x|\rangle_\tau$ against τ/τ_η, where the Kolmogorov time scale $\tau_\eta = (\nu/\varepsilon)^{1/2}$ and length scale η are taken on the centerline at the time when the fluid particles are seeded. The viscous superlayer (VSL) and the turbulent sublayer (TSL) estimated from the Eulerian statistics are indicated in the figure.

with the interface structure by plotting the Lagrangian statistics, which is a function of τ, against $\langle \delta x \rangle_\tau$.

The separation vector $\delta x(\tau)$, a fluid particle location relative to a marker of the irrotational boundary, changes as

$$\frac{d\delta x(\tau)}{d\tau} = \delta u(\tau) \equiv u(\tau) - u_\mathrm{I}(\tau), \tag{8}$$

where δu is the fluid particle velocity in relation to the velocity of the marker of the irrotational boundary, and is simply referred to as the relative velocity. The dot product of Eq. (8) with δx yields the following equation [32]:

$$\frac{d\delta x^2}{d\tau} = 2\int_0^\tau \delta u(\tau) \cdot \delta u(\tau')d\tau'. \tag{9}$$

The relative velocity can be decomposed into the two components: the irrotational boundary propagation velocity (u_P) and the fluid velocity difference ($u - u_0$) between the fluid particle and the location of the marker of the irrotational boundary:

$$\delta u(\tau) = -u_\mathrm{P}(\tau) + (u(\tau) - u_0(\tau)). \tag{10}$$

For small τ, we can assume that the fluid particles are located in the proximity of the irrotational boundary [14], and the fluid velocity is almost the same between the locations of the fluid particle and the marker of the irrotational boundary. Then, $|u_\mathrm{P}| \gg |u - u_0| \approx 0$, and the relative velocity can be approximated by $\delta u(\tau) \approx -u_\mathrm{P}(0)$ [33]. Thus, Eq. (9) is simply,

$$\frac{d\delta x^2}{d\tau} = 2\int_0^\tau (u_\mathrm{P}(0) \cdot u_\mathrm{P}(0))dt' = 2v_\mathrm{E}^2\tau. \tag{11}$$

Integration of Eq. (11) yields $\delta x^2 = v_\mathrm{E}^2\tau^2$, where v_E is taken at $\tau = 0$. Thus, the Lagrangian conditional root-mean-squared distance changes with

$$\langle \delta x^2 \rangle_\tau^{1/2} = \langle v_\mathrm{E}^2 \rangle_{\tau=0}^{1/2}\tau \quad \text{(for small } \tau\text{)}. \tag{12}$$

It was shown that the propagation velocity scales with the Kolmogorov velocity [14]. By contrast, the fluid velocity difference between two points can be much larger in turbulent flows. Therefore, once the fluid particle has reached far away from the irrotational boundary, the fluid velocity difference can be large compared with the propagation velocity. Then, in the

case of $\delta u \approx u - u_0$, the fluid particle movement in relation to the irrotational boundary is described as the two-particles dispersion problem [34]. Similar to Richardson's law for the relative diffusion, under the assumption that δx changes by eddies of size $\delta x(\tau)$ [35], we can obtain the following relationship in the self-similar regime:

$$\left\langle \delta x^2 / \varepsilon \right\rangle_\tau^{1/2} = C\tau^{3/2} \quad \text{(for large } \tau\text{),} \tag{13}$$

where C is a constant, and the mean kinetic energy dissipation rate ε is time dependent. Here, we use ε obtained in the turbulent core region. This expression can be obtained with the modified Richardson's law for decaying turbulence [36,37] in the self-similar regime, where $\varepsilon(t)$ decays as $\varepsilon(t) \sim t^{-n}$.
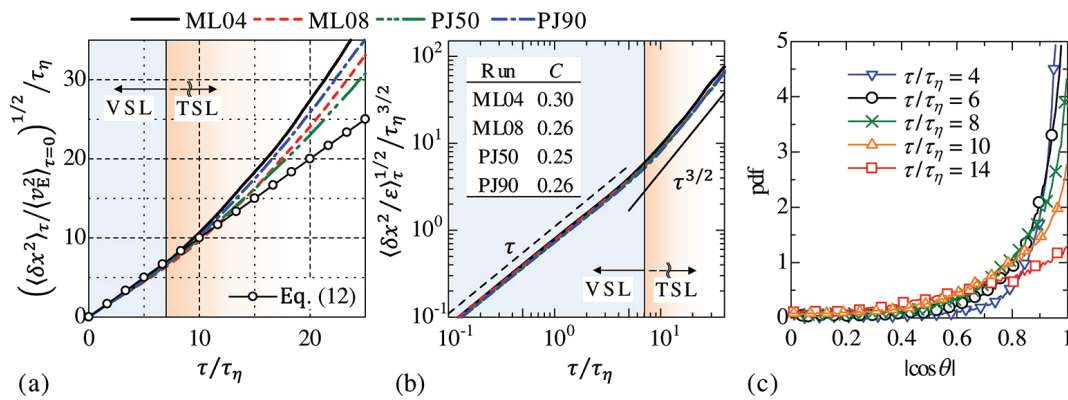

Figure 10. The scalings for the mean-squared distance between entrained fluid particle and irrotational boundary. (a) The ballistic evolution in the initial stage of the entrainment. (b) The modified Richardson-like scaling for the mean-squared distance. The viscous superlayer (VSL) and the turbulent sublayer (TSL) estimated from the Eulerian statistics are indicated in (a) and (b). (c) Pdf of the cosine of the angle between δx and the irrotational boundary normal $\mathbf{n}$.

Figure 10(a) shows $\left\langle \delta x^2 \right\rangle_\tau^{1/2}$ for comparison between the DNS results and Eq. (12). For $\tau/\tau_\eta \lesssim 10$, Eq. (12) well predicts $\left\langle \delta x^2 \right\rangle_\tau^{1/2}$. Thus, within the viscous superlayer ($\tau/\tau_\eta \leq 7$), δx is changed by the irrotational boundary propagation with only a negligible influence of the fluid velocity. Since the irrotational boundary is located at the outer edge of the T/NT interface, where the enstrophy grows by the viscous diffusion with only a negligible influence of vortex stretching, the outward enstrophy diffusion causes the fluid particles to reach the turbulent sublayer. **Figure 10(b)** shows $\left\langle \delta x^2 / \varepsilon \right\rangle_\tau^{1/2}$ against τ. The plots of $\left\langle \delta x^2 / \varepsilon \right\rangle_\tau^{1/2}$ are similar in all DNS presented in this study. For $\tau \approx 0$, Eq. (12) yields $\left\langle \delta x^2 / \varepsilon \right\rangle_\tau^{1/2} \propto \tau$. Both scaling laws, Eqs. (12) and (13), are recovered in all simulations. The relationship for larger τ, Eq. (13), is satisfied from $\tau/\tau_\eta \approx 9$, which is the time slightly after the particles reach the turbulent sublayer (see **Figure 9(b)**). Eq. (13) is valid for larger τ/τ_η, including the entire turbulent sublayer. The values of the constant C, obtained with the least-squares methods, are between 0.25 and 0.30 as displayed in **Figure 10(b)**. The important assumption behind the relationship, Eq. (13), is that the fluid particle movement in relation to the irrotational boundary is caused solely by eddies of size

δx without viscous effects nor eddies with different sizes. The entrained particles within the turbulent sublayer, $\delta_v \lesssim \delta x \lesssim \delta_v + \delta_\omega$, obey Eq. (13), indicating that the particle movement is caused by the small-scale eddy motions whose size is from δ_v to $\delta_v + \delta_\omega$. These small-scale eddies with core radius of about 5η ($\approx \delta_v$) were found within the turbulent sublayer as intense vorticity structures [38].

Figure 10(c) shows the pdf of the cosine of the angle between the separation vector δx and the irrotational boundary normal $\boldsymbol{n}$. Because the particle location within the viscous superlayer changes with the irrotational boundary propagation, whose direction is given by $\boldsymbol{n}$, the particle in the viscous superlayer stays in the normal direction of the irrotational boundary. This is confirmed by a large peak in the pdf associated with a parallel alignment of δx and $\boldsymbol{n}$.
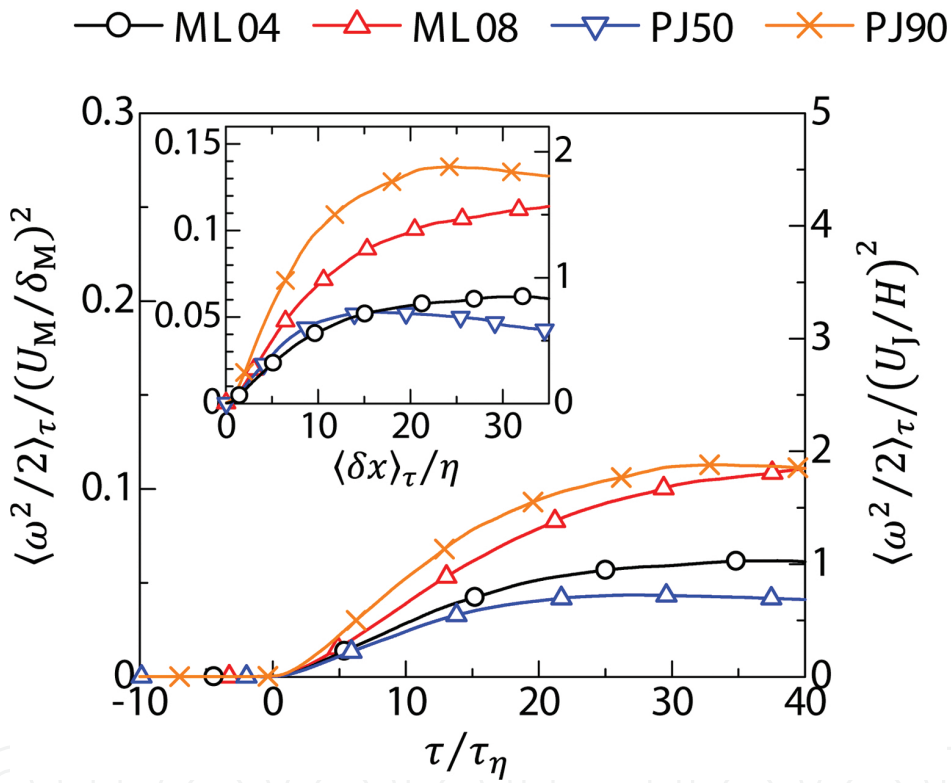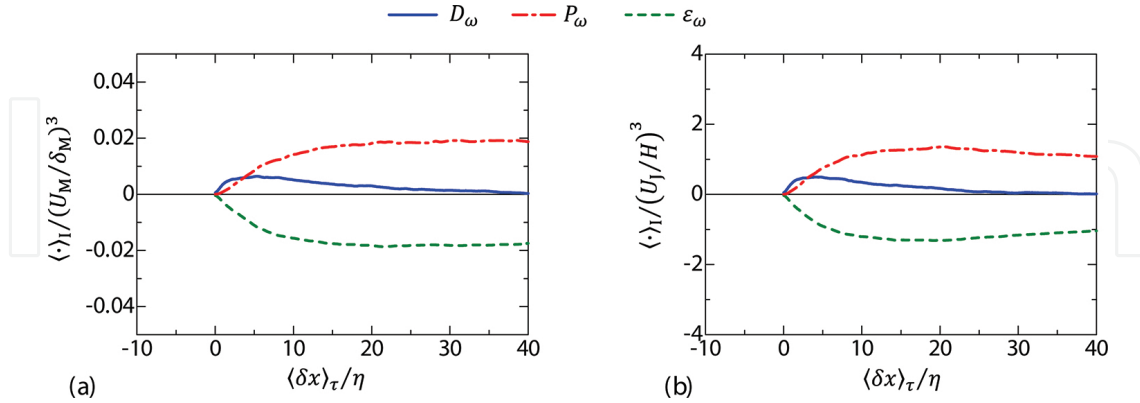

Figure 11. Lagrangian conditional mean enstrophy $\langle \omega^2/2 \rangle_\tau$. The inset plots $\langle \omega^2/2 \rangle_\tau$ against the mean distance between the particle and the irrotational boundary.

Figure 11 shows the Lagrangian conditional mean enstrophy $\langle \omega^2/2 \rangle_\tau$, where the inset plots $\langle \omega^2/2 \rangle_\tau$ against $\langle \delta x \rangle_\tau$ for comparison with the Eulerian statistics in **Figure 5**. Once the particle moves into the T/NT interface layer, the enstrophy begins to grow. The inset shows that even after the particle reaches deep inside the turbulent region, the mean enstrophy on the particle path is much smaller than the Eulerian conditional mean enstrophy in **Figure 5(a)**. It should be noted that the Lagrangian statistics are obtained only from the fluid being entrained, whereas the Eulerian statistics contain the contributions from the entrained fluid and the fluid from the turbulent core region. This makes differences between the Lagran-

gian and Eulerian statistics, and the Eulerian statistics are not enough for studying the entrainment process across the T/NT interface layer.


Figure 12. Lagrangian conditional mean enstrophy budget of the entrained particles plotted against the mean distance $\langle \delta x \rangle_\tau$ between the particle and the irrotational boundary. (a) ML08 and (b) PJ90.

Figure 12 shows the Lagrangian conditional statistics of the enstrophy budget, where again the Lagrangian statistics are plotted against $\langle \delta x \rangle_\tau$ for comparison with the Eulerian statistics in **Figure 6**. Qualitative differences can be found between the Eulerian and Lagrangian conditional means of D_ω. The Eulerian $\langle D_\omega \rangle_I$ displays both positive and negative values indicating an outward mean enstrophy transport, whereas the Lagrangian $\langle D_\omega \rangle_\tau$ is positive even for large $\langle \delta x \rangle_\tau$. Thus, although the fluid being entrained possesses an important level of enstrophy in the T/NT interface layer, the enstrophy transport toward the non-turbulent region is hardly associated with this entrained fluid. The Lagrangian enstrophy production and dissipation terms are smaller than their corresponding Eulerian counterparts. Note that these terms are proportional to the enstrophy, and this difference between Lagrangian and Eulerian statistics seems to be due to a smaller enstrophy level on the entrained particle path.

Figure 13(a) compares the Eulerian and Lagrangian conditional averages of the second invariant of velocity gradient tensor $Q = (\omega_i \omega_i - 2S_{ij}S_{ij})/4$. A large positive value of Q implies the predominance of vorticity over the strain while its negative value is related to where dissipation is dominant. The vortex core region of an eddy often has positive Q while negative Q appears around the core region [35]. The Eulerian $\langle Q \rangle_I$ has a negative peak near the irrotational boundary and a large positive peak inside the turbulent region. However, the Lagrangian $\langle Q \rangle_\tau$ is negative even for large $\langle \delta x \rangle_\tau$ in the turbulent core region. The third invariant of the velocity gradient tensor is defined by $R = -(S_{ij}S_{jk}S_{ki}/3 - \omega_i S_{ij}\omega_j/4)$, and the joint pdf of Q and R has been used for investigating the local flow topology in various turbulent flows [39–41]. **Figure 13(b) and (c)** compares the joint pdf of Q and R obtained as the Eulerian and Lagrangian statistics in the turbulent sublayer. Both Eulerian and Lagrangian pdfs show a "teardrop" shape similar to various turbulent flows, but a difference is found for large positive Q; the probability of finding intense values of $Q \gg 0$ is smaller in the Lagrangian pdf than in the Eulerian counterpart. These statistics of Q show that although there are regions with $Q \gg 0$ within the T/NT interface layer, the fluid particles being entrained tend to circumvent these

regions. The regions with $Q \gg 0$ can be related to the core of the intense eddies. Thus, a circular motion induced by these eddies may explain this entrained particle path.
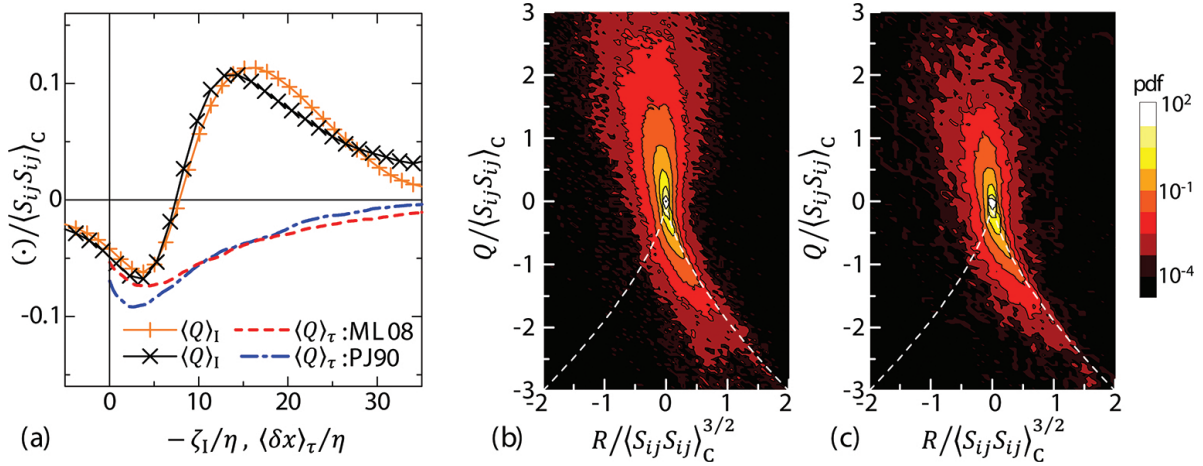
Figure 13. (a) Comparison between the Eulerian and Lagrangian conditional averages of the second invariant of the velocity gradient tensor ($\langle Q \rangle_\text{I}$ and $\langle Q \rangle_\tau$, respectively). The Lagrangian conditional average is plotted against $\langle \delta x \rangle_\tau$. Joint pdf of the second and third invariants of the velocity gradient tensors in (b) Eulerian and (c) Lagrangian statistics. Invariants are normalized by the mean strain product on the centerline $\langle S_{ij} S_{ij} \rangle_\text{C}$ at the time when the particles are seeded.

4. Conclusion

The DNS of planar jets and mixing layers was performed for investigating the vorticity dynamics near the T/NT interface. The outer edge of the T/NT interface layer, irrotational boundary, is detected as an isosurface of the vorticity magnitude. The Eulerian and Lagrangian statistics were investigated in this study. The former was calculated conditioned on the distance from the irrotational boundary. For investigating the Lagrangian properties of the entrainment, a large number of fluid particles are seeded in the non-turbulent region of the self-similar regime. The Lagrangian statistics were calculated as a function of time elapsed after the particle crosses the irrotational boundary. Furthermore, a marker of the irrotational boundary is also tracked with the velocity of the enstrophy isosurface movement, and is used for examining the fluid particle location within the T/NT interface layer.

The Eulerian conditional mean enstrophy and its budget showed that the T/NT interface is a layer with the thickness of about 15η, and consists of the viscous superlayer and the turbulent sublayer with the thickness of $\delta_v \approx 4\eta$ and $\delta_\omega \approx 11\eta$, respectively. It was also found that the amplification of the vorticity and scalar gradient is efficient in the turbulent sublayer. The passive scalar exhibits a jump in the T/NT interface layer, where the large scalar dissipation rate appears near the boundary between the viscous superlayer and the turbulent sublayer in all simulations.

The Lagrangian statistics of the entrained particle and the marker of the irrotational boundary showed that it takes about $7\tau_\eta$ for the entrained particle to pass across the viscous superlayer.

The mean-squared distance exhibited two different scalings depending on the location: a ballistic evolution in the viscous superlayer and the Richardson-like scaling for the relative dispersion in the turbulent sublayer. These scalings indicate that the different mechanisms govern the entrained fluid movement between the two layers. A ballistic evolution was explained reasonably based on the irrotational boundary propagation, which arises from the viscous diffusion of vorticity. The Richardson-like scaling implies the importance of inviscid motions of small-scale eddies in the entrainment. The Lagrangian statistics also showed that although the fluid being entrained possesses an important level of enstrophy, it does not contribute, in a mean sense, to the viscous diffusion of vorticity to the irrotational region. Thus, the fluid existing in the turbulent core region plays an important role in the vorticity diffusion near the T/NT interface. The $Q - R$ analysis indicates that the entrained fluid path appears around the core of the small-scale eddy structures related to very large Q.

Acknowledgements

Author details

Tomoaki Watanabe[1*], Koji Nagata[1] and Carlos B. da Silva[2]

*Address all correspondence to: watanabe@nuae.nagoya-u.ac.jp

1 Nagoya University, Nagoya, Japan

2 Instituto Superior Técnico, Universidade de Lisboa, Lisboa, Portugal

References

[1] Thorpe SA. The near-surface ocean mixing layer in stable heating conditions. J. Geophys. Res. 1978; 83:2875–2885. DOI: 10.1029/JC083iC06p02875

[2] Mahrt L. Stratified atmospheric boundary layers. Boundary-Layer Meteorol. 1999; 90:375–396. DOI: 10.1023/A:1001765727956

[3]　Corrsin S, Kistler AL. Free-stream boundaries of turbulent flows. NACA Technical Report No. TN-1244; 1955. DOI: 19930092246

[4]　Taveira RR, da Silva CB. Characteristics of the viscous superlayer in shear free turbulence and in planar turbulent jets. Phys. Fluids 2014;26:021702. DOI: 10.1063/1.4866456

[5]　Bisset DK, Hunt JCR, Rogers MM. The turbulent/non-turbulent interface bounding a far wake. J. Fluid Mech. 2002;451:383–410. DOI: 10.1017/S0022112001006759.

[6]　da Silva CB, Hunt JCR, Eames I, Westerweel J. Interfacial layers between regions of different turbulence intensity. Annu. Rev. Fluid Mech. 2014;46:567–590. DOI: 10.1146/annurev-fluid-010313-141357

[7]　van Reeuwijk M, Holzner M. The turbulence boundary of a temporal jet. J. Fluid Mech. 2014;739:254–275. DOI: 10.1017/jfm.2013.613

[8]　Watanabe T, Sakai Y, Nagata K, Ito Y, Hayase T. Turbulent mixing of passive scalar near turbulent and non-turbulent interface in mixing layers. Phys. Fluids 2015;27:085109. DOI: 10.1063/1.4928199

[9]　Westerweel J, Fukushima C, Pedersen JM, Hunt JCR. Mechanics of the turbulent-nonturbulent interface of a jet. Phys. Rev. Lett. 2005;95:174501. DOI: 10.1103/PhysRevLett.95.174501

[10]　Townsend AA. The Structure of Turbulent Shear Flow. Cambridge University Press; Cambridge 1976.

[11]　Philip J, Meneveau C, de Silva CM, Marusic I. Multiscale analysis of fluxes at the turbulent/non-turbulent interface in high Reynolds number boundary layers. Phys. Fluids 2014;26:015105. DOI: 10.1063/1.4861066

[12]　Holzner M, Lüthi B. Laminar superlayer at the turbulence boundary. Phys. Rev. Lett. 2011;106:134503. DOI: 10.1103/PhysRevLett.106.134503

[13]　Wolf M, Lüthi B, Holzner M, Krug D, Kinzelbach W, Tsinober A. Investigations on the local entrainment velocity in a turbulent jet. Phys. Fluids 2012;24:105110. DOI: 10.1063/1.4761837

[14]　Wolf M, Holzner M, Lüthi B, Krug D, Kinzelbach W, Tsinober A. Effects of mean shear on the local turbulent entrainment process. J. Fluid Mech. 2013;731:95–116. DOI: 10.1017/jfm.2013.365

[15]　de Silva CM, Philip J, Chauhan K, Meneveau C, Marusic I. Multiscale geometry and scaling of the turbulent-nonturbulent interface in high Reynolds number boundary layers. Phys. Rev. Lett. 2013;111:044501. DOI: 10.1103/PhysRevLett.111.044501

[16]　Deo RC, Nathan GJ, Mi J. Similarity analysis of the momentum field of a subsonic, plane air jet with varying jet-exit and local Reynolds numbers. Phys. Fluids 2013;25:015115. DOI: 10.1063/1.4776782

[17] Holzner M, Liberzon A, Nikitin N, Lüthi B, Kinzelbach W, Tsinober A. A Lagrangian investigation of the small-scale features of turbulent entrainment through particle tracking and direct numerical simulation. J. Fluid Mech. 2008;598:465–475. DOI: 10.1017/S0022112008000141

[18] Taveira RR, Diogo JS, Lopes DC, da Silva CB. Lagrangian statistics across the turbulent-nonturbulent interface in a turbulent plane jet. Phys. Rev. E 2013;88:043001. DOI: 10.1103/PhysRevE.88.043001

[19] Watanabe T, da Silva CB, Sakai Y, Nagata K, Hayase T. Lagrangian properties of the entrainment across turbulent/non-turbulent interface layers. Phys. Fluids 2016;28:031701. DOI: 10.1063/1.4942959

[20] Morinishi Y, Lund TS, Vasilyev OV, Moin P. Fully conservative higher order finite difference schemes for incompressible flow. J. Comput. Phys. 1998;143:90–124. DOI: 10.1006/jcph.1998.5962

[21] Kempf A, Klein M, Janicka J. Efficient generation of initial-and inflow-conditions for transient turbulent flows in arbitrary geometries. Flow Turbul. Combust. 2005;74:67–84. DOI: 10.1007/s10494-005-3140-8

[22] Watanabe T, Sakai Y, Nagata K, Terashima O. Experimental study on the reaction rate of a second-order chemical reaction in a planar liquid jet. AIChE J. 2014;60:3969–3988. DOI: 10.1002/aic.14610

[23] Bell JH, Mehta RD. Development of a two-stream mixing layer from tripped and untripped boundary layers. AIAA J. 1990;28:2034–2042. DOI: 10.2514/3.10519

[24] Tanahashi M, Iwase S, Miyauchi T. Appearance and alignment with strain rate of coherent fine scale eddies in turbulent mixing layer. J. Turbulence 2001;2:1–18. DOI: 10.1088/1468-5248/2/1/006

[25] Kitamura T, Nagata K, Sakai Y, Sasoh A, Terashima O, Saito H, Harasaki T. On invariants in grid turbulence at moderate Reynolds numbers. J. Fluid Mech. 2014;738:378–406. DOI: 10.1017/jfm.2013.595

[26] Uberoi MS, Freymuth P. Turbulent energy balance and spectra of the axisymmetric wake. Phys. Fluids 1970;13:2205–2210. DOI: 10.1063/1.1693225

[27] Attili A, Cristancho JC, Bisetti F. Statistics of the turbulent/non-turbulent interface in a spatially developing mixing layer. J. Turbulence 2014;15:555–568. DOI: 10.1080/14685248.2014.919394

[28] da Silva CB, Taveira RR. The thickness of the turbulent/nonturbulent interface is equal to the radius of the large vorticity structures near the edge of the shear layer. Phys. Fluids 2010;22:121702. DOI: 10.1063/1.3527548

[29] Smyth WD. Dissipation-range geometry and scalar spectra in sheared stratified turbulence. J. Fluid Mech. 1999;401:209–242. DOI: 10.1017/S0022112099006734

[30] Tsinober A. An informal conceptual introduction to turbulence. ***Springer; Berlin 2009. DOI: 10.1007/978-90-481-3174-7

[31] Yang Y, Wang J, Shi Y, Xiao Z, He XT, and Chen S. Acceleration of passive tracers in compressible turbulent flow. Phys. Rev. Lett. 2013;110:064503. DOI: 10.1103/PhysRevLett.110.064503

[32] Batchelor GK. The application of the similarity theory of turbulence to atmospheric diffusion. Q. J. R. Meteorol. Soc. 1950;76:133–146. DOI: 10.1002/qj.49707632804

[33] Watanabe T, Sakai Y, Nagata K, Ito Y, Hayase T. Vortex stretching and compression near the turbulent/nonturbulent interface in a planar jet. J. Fluid Mech. 2014;758:754–785. DOI: 10.1017/jfm.2014.559

[34] Salazar JPLC, Collins LR. Two-particle dispersion in isotropic turbulent flows. Annu. Rev. Fluid Mech. 2009;41:405–432. DOI: 10.1146/annurev.fluid.40.111406.102224

[35] Davidson PA. Turbulence: An Introduction for Scientists and Engineers. Oxford ***University Press; Oxford 2004.

[36] Larcheveque M, Lesieur M. The application of eddy-damped Markovian closures to the problem of dispersion of particle pairs. J. Méc. 1981;20:113–134. DOI: 10.1007/978-3-540-32603-8_ 44

[37] Nelkin M, Kerr RM. Decay of scalar variance in terms of a modified Richardson law for pair dispersion. Phys. Fluids 1981;24:1754–1756. DOI: 10.1063/1.863597

[38] da Silva CB, dos Reis RJN, Pereira JCF. The intense vorticity structures near the turbulent/non-turbulent interface in a jet. J. Fluid Mech. 2011;685:165–190. DOI: 10.1017/jfm.2011.296

[39] Soria J, Sondergaard R, Cantwell BJ, Chong MS, Perry AE. A study of the fine-scale motions of incompressible time-developing mixing layers. Phys. Fluids 1994;6:871–884. DOI: 10.1063/1.868323

[40] Blackburn HM, Mansour NN, Cantwell BJ. Topology of fine-scale motions in turbulent channel flow. J. Fluid Mech. 1996;310:269–292. DOI: 10.1017/S0022112096001802

[41] Zhou Y, Nagata K, Sakai Y, Suzuki H, Ito Y, Terashima O, Hayase T. Development of turbulence behind the single square grid. Phys. Fluids 2014;26:045102. DOI: 10.1063/1.4870167